Electronic Supplementary Material (ESI) for Journal of Materials Chemistry C.
This journal is © The Royal Society of Chemistry 2022

Supporting Information

Electrochemically Driven Dual Bipolar Resistive Switching in $LaNiO_3/SmNiO_3$/NSTO Heterostructures Fabricated Through Selective Area Epitaxy

Yong Zhang, *[†,‡] *Ming Liu,*[†,‡] *Chunrui Ma,*[‡] *Lu Lu,*[†,‡] and *Chuan Yu Han*[§]

†School of Microelectronics & Key Lab of Micro-Nano Electronics and System Integration of Xi'an City, Xi'an Jiaotong University, Xi'an 710049, China

‡State Key Laboratory for Mechanical Behavior of Materials, Xi'an Jiaotong University, Xi'an 710049, China

§School of Microelectronics, Faculty of Electronics and Information Engineering, Xi'an Jiaotong University, Xi'an 710049, China

Estimate roughly the amount of oxygen vacancies in epitaxial nickelate films: For the increase of the parameter c-axis lattice constant and unit-cell volume *V* in nickelate thin films, it can be account for the large concentration of oxygen vacancies. To estimate roughly the amount of oxygen vacancies, we directly associate the lattice expansion with the combined effect of chemical strain and misfit strain. The strained c-axis lattice constants (c_{est}) due to misfit strain can be estimated from the Yong's modulus by taking into account Poisson's Ratio $\nu \approx 0.27$[1]. The out-of-plane chemical strain S_{chem} can be calculated from the difference between the experimental c-axis lattice constants (c_{expt}) and c_{est}. To check feasibility of such strain magnitude, we considered that the out-of-plane chemical strain is induced by the out-of-plane dipoles with the concentration N_{DC} and roughly equals to[2]

$$S_{chem} \approx (D_1 N_{DC})/c_{11}$$

where D_1, c_{11} are dipole tensor along the Ni-Vo-Ni direction and elastic constant of the film material, respectively. For $D_1 \approx 5$ eV[3] and $c_{11} \approx 405$ GPa[1], the estimated N_{DC} for different nickelate thin films are shown in Table 1. It can be found that the N_{DC} is reasonable compared to the concentration of oxygen atoms 5.30×10^{28} m^{-3} in stoichiometric $SmNiO_3$. Specially, according to the discussion in Ref[4], the amount of oxygen vacancies that can be detected by standard lab-tools like XRD is in the high-concentration regime ($10^{27}cm^{-3} \leq N_{DC} \leq 10^{28}cm^{-3}$), which is consistence with the values calculated here.

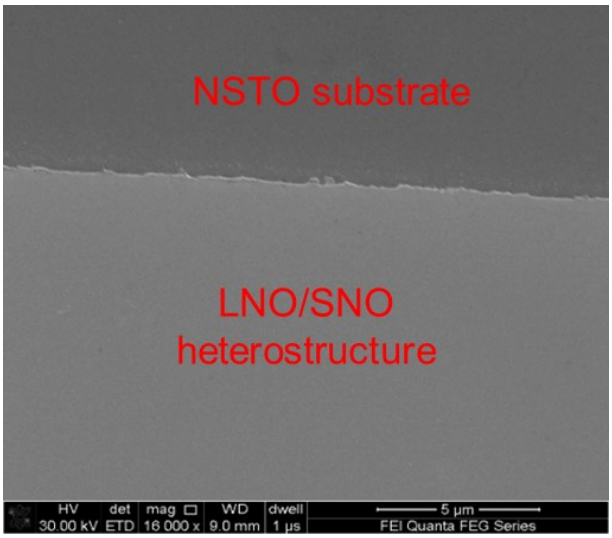

Fig. S1 The LNO/SNO heterostructure fabricated on the NSTO substrate with well-defined edge is verified in the magnified SEM image.

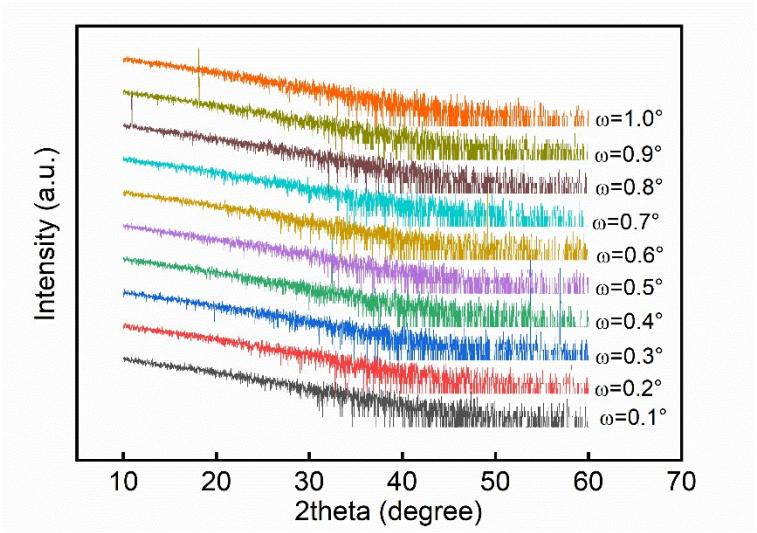

Fig. S2 Grazing Incidence X-ray diffraction (GIXRD) patterns of epitaxial LNO/SNO/NSTO heterostructure with different incident angles (0.1°~1°).

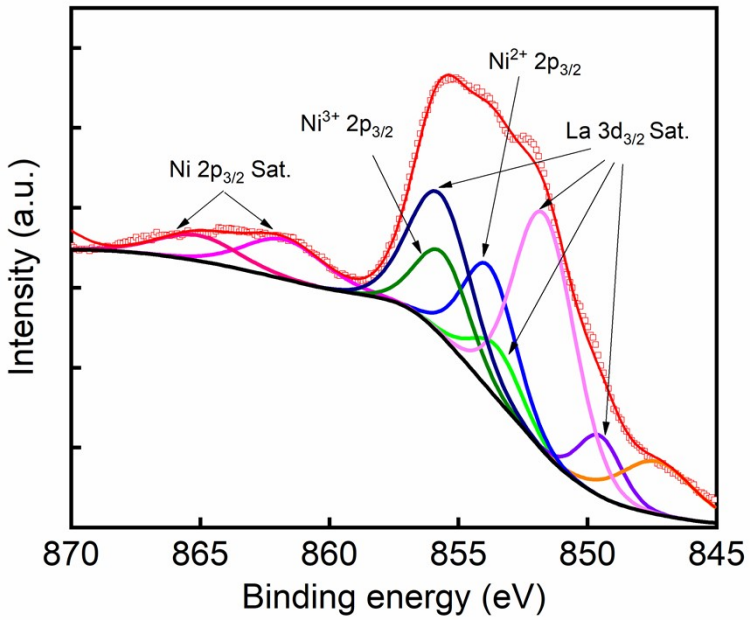

Fig. S3 Deconvolution analysis of La 3d and Ni $2p_{3/2}$ XPS signal of the LNO/SNO/NSTO heterostructure. The scattered points refer to the raw data, the thin solid lines correspond to the spectral components and thick red line is the spectra envelope. The measured lines can be well fitted with La $3d_{3/2}$ and Ni $2p_{3/2}$ spectra components. Specially, it can be found that the percentage of Ni^{2+} in the total Ni ions are rather large, indicating that high concentrations of oxygen vacancies are introduced to the heterostructure.

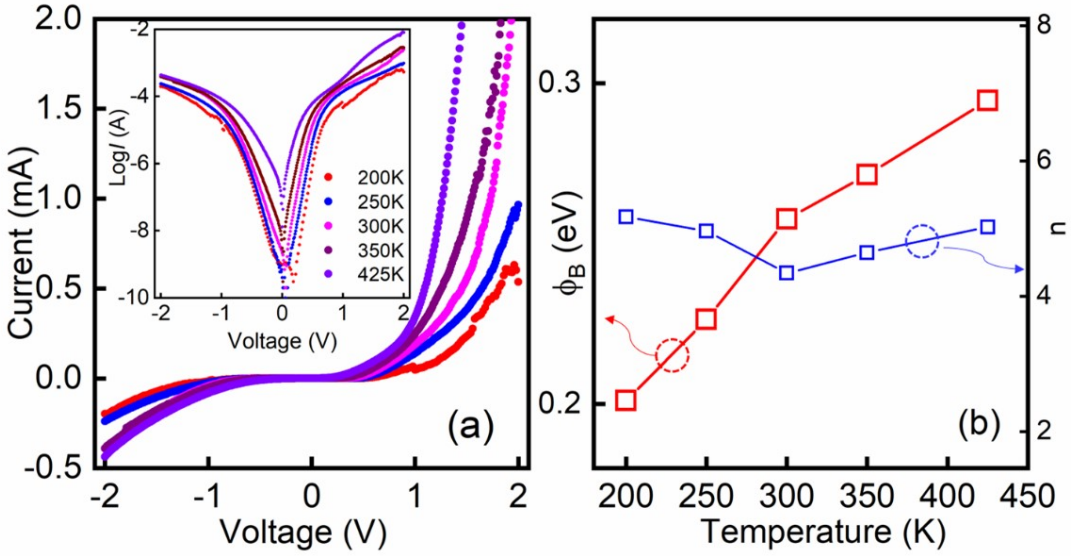

Fig. S4 (a) *I-V* characteristics of a 400×400 μm² LNO/SNO/NSTO heterostructure at several temperatures (425, 350, 300, 250, and 200 K from the left to the right), which show a highly rectifying behavior in the measured voltage range. Inset is Semi-

logarithmic plot of the same *I-V* characteristic at several temperatures and a linear relationship in the intermediate-bias voltage is observed. (b) Temperature dependence of the barrier height Φ_B, and the ideality factor n. The barrier height Φ_B is found to decrease from about 0.3 eV at 425 K to small value of 0.2 eV at the lowest temperatures and the ideality factor n fluctuates within a narrow range (n~5) in the investigated temperatures range.

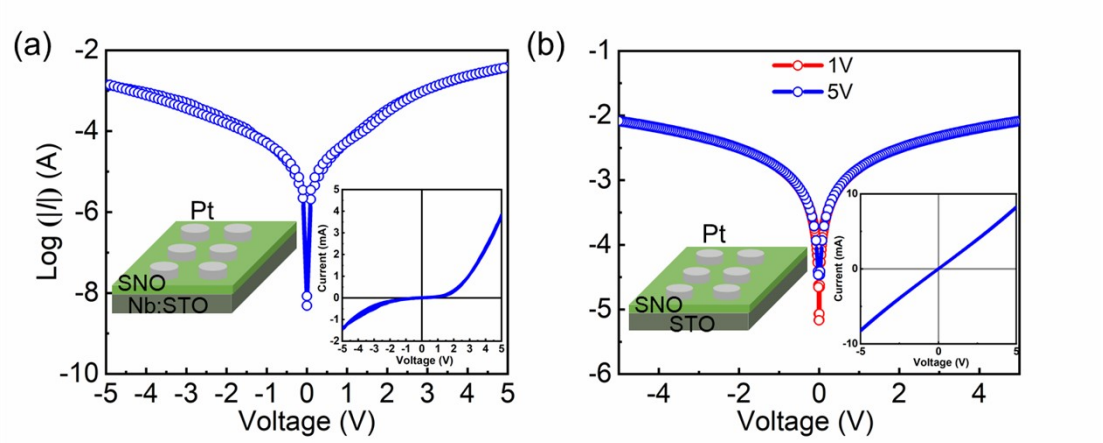

Fig. S5 (a) *I-V* characteristics of the Pt/SNO/NSTO heterostructure plotted in semilog scale and no *I-V* hysteresis characteristics is observed. The left inset is a schematic of the device with Pt electrode contact pads (150×150 μm^2 in size) depositing on the SNO film grown on NSTO substrate, and the right inset is the same *I-V* curve in linear scale, which exhibits good rectifying *I-V* characteristics. (b) In-plane two-probe electrical characteristics between two Pt electrode contact pads. The left inset schematically shows the device with Pt electrode contact pads (150×150 μm^2 in size) depositing on the SNO film grown on undoped STO substrate, and the right inset is the same *I-V* curve in linear scale, which shows a linear *I-V*, demonstrating that the Pt/SNO interface is ohmic and the rectifying behavior observed in (a) can be attributed to a Schottky-like barrier formed at the interface between the SNO film and the NSTO substrate.

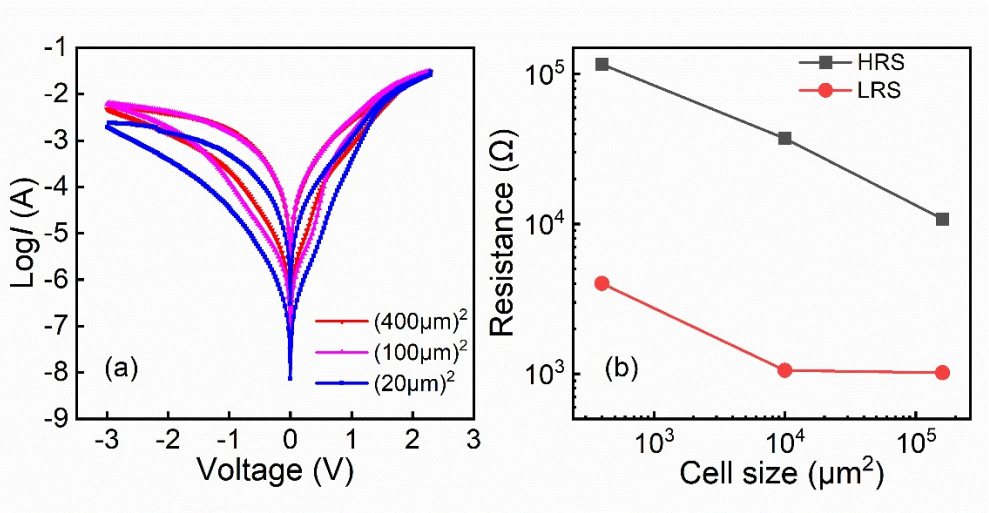

Fig. S6 (a) The *I-V* characteristics of the LNO/SNO/NSTO heterostructures with different cell size plotted in semilog scale and (b) the dependence of the HRS/LRS resistance values on cell size. Resistance was calculated by Ohm's law at a read voltage of -0.5 V for both the LRS and the HRS.

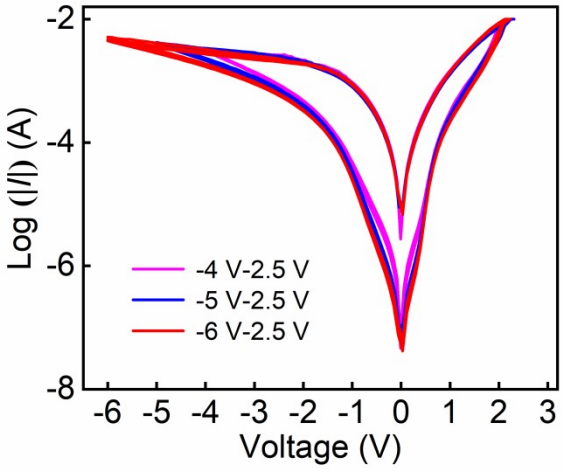

Fig. S7 Different hysteresis *I-V* curves of the heterostructure modulated by different reverse biases.

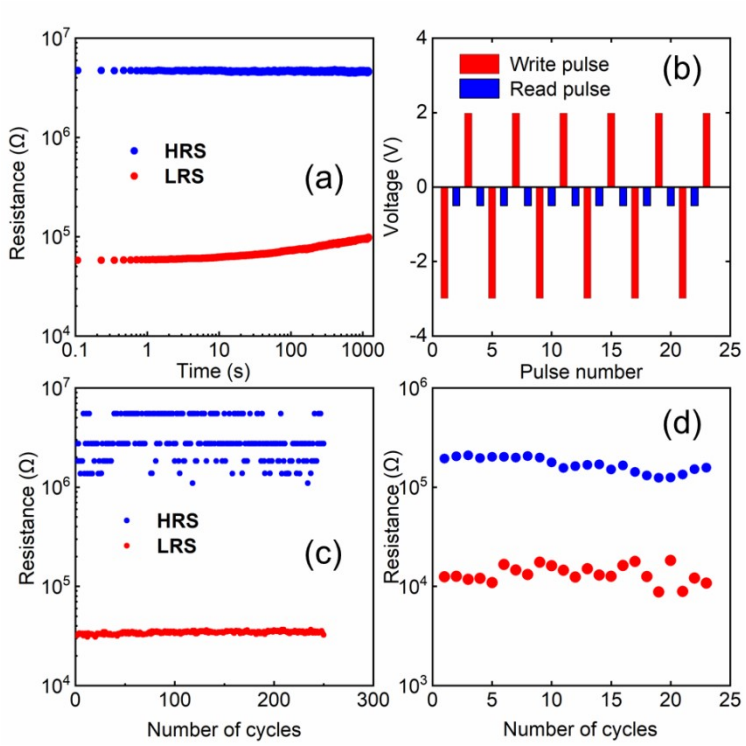

Fig. S8 (a) LRS and HRS retention tests of the F8 BRS under a continuous read voltage of -0.1 V after a forward and reverse bias sweep, respectively. The resulting LRS after the set operation is stable whereas the current in LRS after the reset operation decays with time, eventually returning to HRS. (b) The write and read pulses for endurance test. Endurance tests of (c) 250 cycles for the interface-type BRS at a read bias of -0.55 V and (d) 25 cycles for the abrupt BRS at a read bias of -0.55 V.

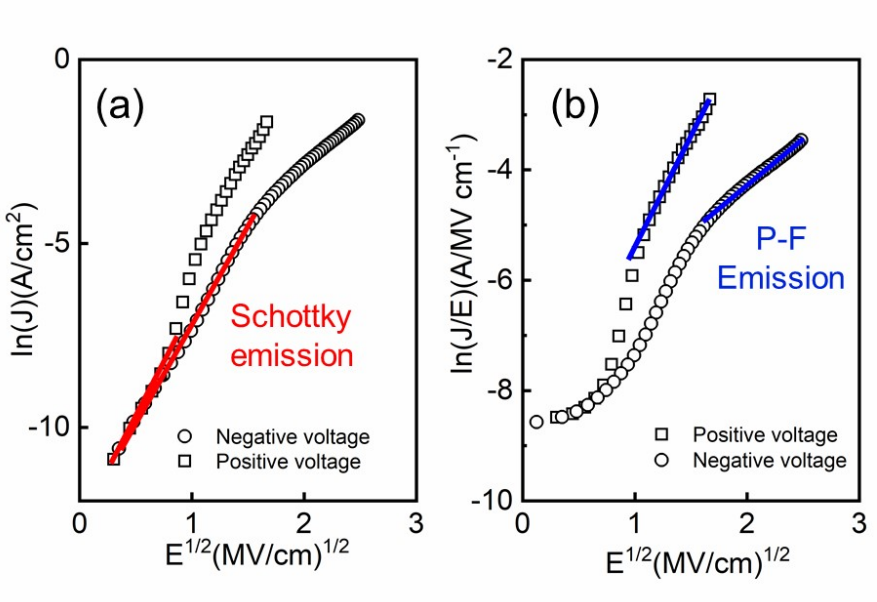

Fig. S9 (a) The ln (J) vs $E^{1/2}$ characteristics and (b) ln (J/E) vs $E^{1/2}$ characteristics of the LNO/SNO/NSTO heterostructure at the positive and negative bias at room temperature.

This non-linear region has good agreement with Schottky emission model in low

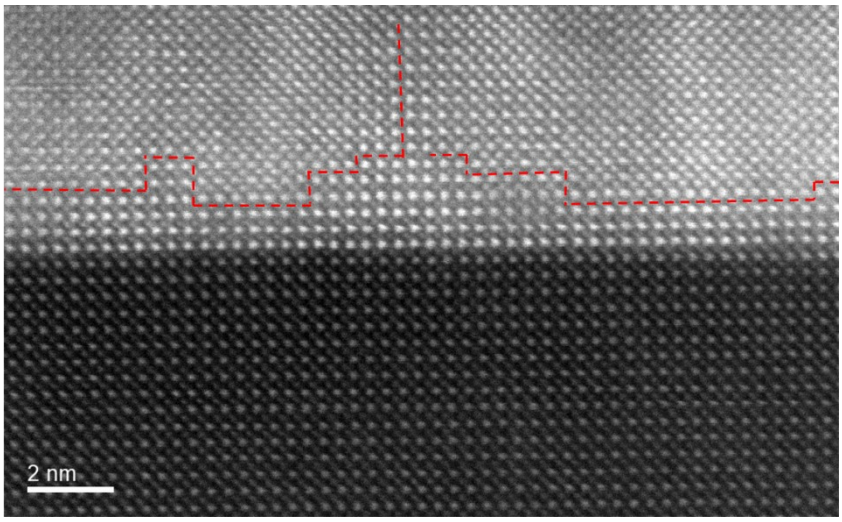

electrical field regime and the P-F emission model in high electrical field regime.

Fig. S10 Cross-sectional HAADF-STEM image of SNO/NSTO interface region. The boundary of the RP faults is denoted by red broken lines in the image. Note that the RP faults are not distributed uniform along the NSTO substrate surface.

Table S1 Summary of the unit cell volumes, volume expansion rates and oxygen vacancies concentration in various perovskite nickelate thin films under in-plane tensile strain.

Film/Substrate	a (Å)	c_{expt} (Å)	c_{est} (Å)	Unit cell volume V_{film} (Å^3)	Volume expansion rate (%)	S_{chem}	N_{DC} (m^{-3})
$SmNiO_3/SrTiO_3$	3.905	3.810	3.751	58.10	7.24	1.56%	7.90×10^{27}
Bilayer $[LaNiO_3/SmNiO_3]/SrTiO_3$	3.905	3.826	3.751	58.34	7.68	1.98%	1.00×10^{28}
Patterned $[LaNiO_3/SmNiO_3]/SrTiO_3$	3.905	3.859	3.751	58.84	8.60	2.85%	1.44×10^{28}

References:

1. Š. Masys and V. Jonauskas, *Comput. Mater. Sci*., 2015, **108**, 153-159.

2. M. Tyunina, O. Pacherova, T. Kocourek and A. Dejneka, *Sci. Rep.*, 2021, **11**, 15247.

3. D. A. Freedman, D. Roundy and T. A. Arias, *Phys. Rev. B,* 2009, **80**, 064108.

4. F. Gunkel, D. V. Christensen, Y. Z. Chen and N. Pryds, *Appl. Phys. Lett.,* 2020, **116**, 120505.